Electrochimica Acta 282 (2018) 194–204

Contents lists available at ScienceDirect

Electrochimica Acta

journal homepage: www.elsevier.com/locate/electacta

In situ synthesized SrF_2/polyvinylidene fluoride nanocomposite film based photo-power cell with imperious performance and stability

Farha Khatun [a], Pradip Thakur [b, *], Nur Amin Hoque [a], Arpan Kool [a], Swagata Roy [a], Prosenjit Biswas [a], Biswajoy Bagchi [c], Sukhen Das [a, **]

[a] Department of Physics, Jadavpur University, Kolkata, 700032, India
[b] Department of Physics, Netaji Nagar College for Women, Kolkata, 700092, India
[c] Department of Medical Physics and Biomedical Engineering, University College London, London, United Kingdom

ARTICLE INFO

Article history:
Received 1 March 2018
Received in revised form
29 May 2018
Accepted 7 June 2018

Keywords:
PVDF
SrF_2
Dielectric
Power
Storage
Stability

ABSTRACT

A self-charged photo-power cell, named as light sensitive energy storage device has been developed in a simplified way for application as a portable photo-charged power bank. The Photo-Power Cell is fabricated by assembling a photoelectrode (FTO) involving a dye-sensitized solar part as photo-electrons generator, combined with the electroactive and high dielectric SrF_2-PVDFNCfilm as storage unit. Electroactive β phase crystallization and large interfacial polarization between the SrF_2 NPs and poly (vinylidene fluoride) matrix result in high dielectric value ~ 5141 of the nanocomposite film. The device is charged by up to 1.48 V under visible light illumination (~110 mW/cm^2) with a constant discharge current density ~1.64 mA/cm^2. The photogenerated charge and power density of the photo-power cell are found to be ~24.3 W/m^2 and 2400 C/m^2 respectively. Our photo-power cell shows maximum areal specific capacitance ~1600 F/m^2 with 92% energy storage efficiency. The achieved overall efficiency (%) is found ~ 2.57. The charging-discharging stability is also tested for a long time span of 12 weeks. The efficacy and durability of our fabricated device has also been demonstrated by glowing up 24 commercially available blue light emitting diodes for 10 days with same intensity by charging one time under light.

1. Introduction

A major concern for sustained development of our modern society is renewable energy creation and reservation [1]. Replacement of conventional fuel sources like coal, petrol, gas etc. is very important for the overall improvement of global economy due to the increased ecological impairment and fast exhaustion of fuel resources [2–5].Under this circumstances, the researchers worldwide are looking for a simple, cost-effective and scalable mechanism for clean and reliable energy extraction from natural energy resources like wind, sunlight, water, biomass energies etc. with simultaneous storage of that energy in the same unit [6–8].

Recently, fabrication of piezoelectric nanogenerators, solar cells, metal O_2 batteries have proved very promising for harnessing electrical energy from clean and renewable sources like living systems, mechanical, solar and chemical respectively [9,10]. More-recently hybrid devices capable of both electrical energy generation and storage with superior power density and stability have been reported with success [11–13]. In such hybrid devices, an extra storage unit is not necessary, which makes them not only more cost-effective but also promising in the field of portable electronics.

Development of nanocomposite materials based photo-power units have been gaining interest among researchers for example, a poly (vinylidene fluoride) (PVDF)/ZnO nanocomposites (NCs) based photo-power unit was proposed by Zhang et al. (energy density $E = 1.4$ mW h kg^{-1}) [14]. Later, perovskite structure and dye-sensitized solar cell based few photovoltaic cells with storage ability was reported [15–17]. Wee et al. suggested an organic photovoltaic integrated with carbon nanotube based supercapacitor with low power loss [18]. Power density, storage stability and durability of an integrated photo-power unit are the necessary factors for practical utilization. Proper designing and integration of dye-sensitized solar energy conversion part and high dielectric polymeric film into a single unit has potential to surpass the critical deficiency associated with traditional power utilization [14].Our

* Corresponding author.
** Corresponding author.
E-mail addresses: pradipthakurju@gmail.com (P. Thakur), sdasphysics@gmail.com (S. Das).

https://doi.org/10.1016/j.electacta.2018.06.054
0013-4686/

previous attempts of designing such type of two electrode photo-power cells with high dielectric PVDF composites demonstrated both energy conversion as well as storage in one unit [19,20].

Electroactive and high dielectric polymer NCs have been progressively appreciated by the scientists due to their versatile utilization in the domain of piezoelectric nanogenerators, capacitors, thin film transistors, grid levelling, rail runs, non-volatile memories, sensors, actuators and also in biomedical fields [21–24].Though, extensive researches have been carried out to design PVDF based piezoelectric nanogenerators [25,26], but the utilization of high dielectric PVDF or PVDF based NCs as energy storage unit in hybrid photo-power banks are very limited to the best of our knowledge.

PVDF ($[-CH_2-CF_2-]_n$) and its copolymers are very promising electroactive semicrystalline thermoplastic polymer with superior piezoelectric, pyroelectric, ferroelectric properties, thermal stability and chemical resistance. Five crystalline polymorphic phases α, β, γ, δ *and* ε have been recognized in PVDF amongst which β phase is the most electroactive [27–30]. Existence of matrix of the orthorhombic unit cells and *all trans*(TTTT) planar zigzag chain conformation in electroactive β polymorph leads to optimum dipolar moment per unit cell and consequent highest piezoelectric, ferroelectric, pyroelectric and dielectric properties in comparison to the other phases of PVDF [27,28].

Herein, we have designed a cost-effective, simple, highly efficient and durable two electrode light sensitive energy storage device (LSESD) by using *in situ* synthesized SrF_2nanoparticles (NPs) incorporated giant dielectric PVDF thin film (named as PSR) associated with an organic dye phenosafranine-polyvinyl pyrrolidone (PSF-PVP) film and zinc oxide (ZnO) and titanium dioxide (TiO_2) NPs as a solar part (Fig. 1). This solar component and the high dielectric PSR film forms the key part of solar energy conversion and photo-generated electrical energy storage respectively.

2. Experimental

2.1. Materials

The materials that are used in our present work are poly (vinylidenefluoride) (PVDF) pellets (Aldrich, Germany. M_w: 275,000 GPC, M_n : 71,000), Strontium nitrate (CDH, India), Ammonium fluoride (Merck, India), dimethyl sulfoxide, (DMSO) (Merck, India), polyvinyl pyrrolidone (PVP) (Loba Chemie), ZnO and TiO_2 NPs, Ortho-phosphoric acid (H_3PO_4) (Merck, India), Phenosafranine (PSF) (Sigma Aldrich, Germany), FTO coated glass (Sigma Aldrich, Germany).

2.2. In situ synthesis of SrF_2/PVDF nanocomposite films

Initially, a solution of PVDF (4%) in DMSO was prepared by

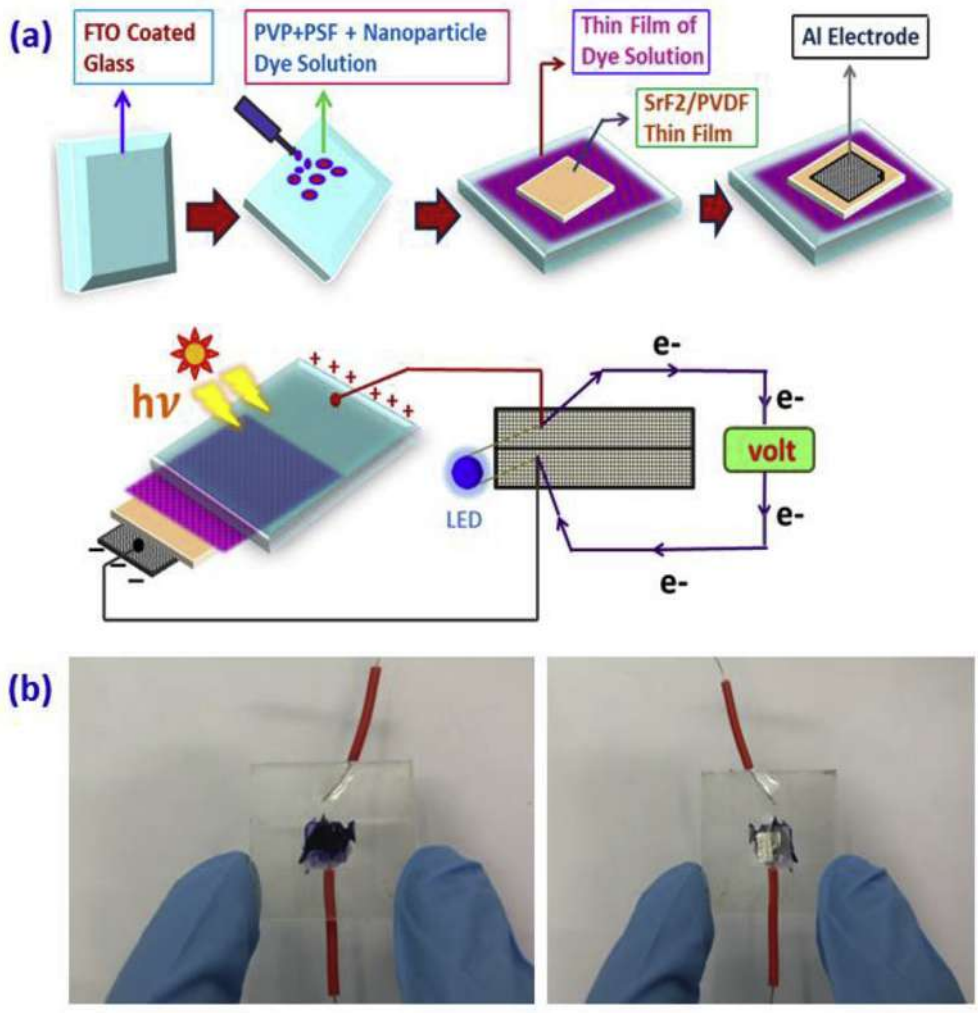

Fig. 1. (a) Schematic diagram of the fabrication process of the LSESD. (b) Digital image of the LSESD.

continuous stirring at 60 °C.Then, $Sr(NO_3)_2$ and NH_4F were dissolved in PVDF-DMSO solution separately with different molar concentrations (0.01–0.2 (M)) and corresponding double molar concentrations respectively. Addition of NH_4F into $Sr(NO_3)_2$/PVDF solution resulted in gradual *in situ* formation of SrF_2 NPs in the polymeric solution under magnetic stirring at 80 °C.The SrF_2/PVDF NC films were obtained by solvent casting method via evaporation of the solvent in an oven at 80 °C in a dust free atmosphere for 24 h. Simultaneously, pure PVDF film was also prepared under same conditions. For characterization, all the films were stored in a vacuum desiccator. The average thickness of the films was ~20 μm. The different concentrations of SrF_2 NPs in PVDF matrix (0.01 M – 0.2 M) have been tabulated in Table S1 (See supporting information).

2.3. Photo-power cell fabrication

Firstly, the dye solution (20 mg/ml PSF and 100 mg/ml ZnO and TiO_2 NPs in 10% mass PVP solution) were prepared in distilled water by continuous stirring at room temperature. Next the dye solution is drop casted on a FTO coated glass (well cleaned by acetone) and vacuum desiccated at ambient temperature (~25 °C) till the solution becomes viscous. Thereafter, the previously prepared PVDF/SrF_2 NC (0.2 M) thin film is placed on the viscous surface and dried at 80 °C for complete removal of water. A counter electrode made of aluminium (using conducting aluminium paste) is pasted on the top of the PVDF/SrF_2 NC (0.2 M) NC film and two Cu wires are connected from either side of the electrode for measurements (Fig. 1). Similarly another device was prepared using the pure PVDF film in place of SrF_2/PVDF NC (0.2 M) film without varying the solar part for comparison purpose.

2.4. Characterization

For the investigation of different phases in the samples an X-ray diffractometer (Model-D8, Bruker AXS Inc, Madison, WI) and Fourier transform infrared spectrophotometer (FTIR-8400 S, Shimadzu) have been used. The fraction of β-phase (F(β)) in SrF_2 incorporated films was calculated from IR spectra using Lambert–Beer law,

$$\boldsymbol{F(\beta)} = \frac{\boldsymbol{A_\beta}}{\left(\frac{\boldsymbol{K_\beta}}{\boldsymbol{K_\alpha}}\right)\boldsymbol{A_\alpha} + \boldsymbol{A_\beta}} \quad (1)$$

where, Aα and Aβ are the absorbance at 764 cm^{-1} and 840 cm^{-1} respectively and K_β ($7.7 \times 10^4\ cm^2\ mol^{-1}$) and K_α ($6.1 \times 10^4\ cm^2\ mol^{-1}$) are the absorption coefficients at the respective wavenumber.

To analyse the crystallization and melting nature of the NCs, we have used a differential scanning calorimeter (DSC-60, Shimadzu (Asia Pacific) Pte. Ltd., Singapore) and TGA (TGA/SDTA851e, Mettler Toledo AG). All the films have been heated from 30 °C to 600 °C at the heating rate of 10 °C/min using ceramic crucibles of capacity 70μl under N_2 atmosphere. The enthalpies (ΔH_m) of fusion or melting enthalpies of the pure and *in situ* synthesized SrF_2/PVDF NC films was obtained with the help of the endothermic peaks of the DSC curves. The degree of crystallinity (X_c) of the samples are calculated by,

$$\boldsymbol{X_c} = \boldsymbol{\Delta H_m}/\boldsymbol{\Delta H_{100\%}} \quad (2)$$

where, ΔH_m is the heat of melting or enthalpy of fusion and $\Delta H_{100\%}$ is the melting enthalpy of 100% crystalline PVDF with a value 104.6 J/gm.

The optical absorption and emission properties of all samples were investigated by a UV–visible spectrometer (Lambda 25, Perkin Elmer, USA and UV - 3101 PC, Shimadzu) and Cary Eclipse fluorescence spectrophotometer (Agilent Technologies) respectively.

The morphological characteristics of the thin films were studied by a field emission electron microscope (FESEM) (INSPECT F50, Netherland).

To study the dielectric properties of the composite samples, a digital LCR meter (Agilent, E4980A) was used. The variation of the capacitance (C) and tangent loss (tan δ) with frequency were recorded in the frequency range 20 Hz to 2 MHz at room temperature applying 1 V ac voltage across the two opposite surfaces of the samples. Dielectric constant (ε) and the ac conductivity (σ_{ac}) of the samples are evaluated using,

$$\boldsymbol{\varepsilon} = \boldsymbol{C}.\boldsymbol{d}/\boldsymbol{\varepsilon_0 A} \quad (3)$$

$$\boldsymbol{\sigma_{ac}} = 2\boldsymbol{\pi f \varepsilon_0}\varepsilon\ tan\delta \quad (4)$$

where, d and A are the thickness and area of the samples respectively and f is the frequency in Hz applied across the samples and ε_0 is the permittivity of the free space with value $8.854 \times 10^{-12} F.m^{-1}$ [27].

The photovoltaic studies of photo-power cell were carried out using a digital multi-meter (Agilent U1252A) and an Electrometer (Keysight- B2985A).

3. Results and discussions

The fabrication of LSESD and its digital photograph have been represented schematically in Fig. 1. We have used the *in situ* SrF_2/PVDF NC thin film as the active material for storing the photo-generated electrons or charge carriers by the adjacent solar part. Our study involves detailed characterization and optimization of the optical and dielectric properties of the *in situ* SrF_2/PVDF NC thin films and then fabrication of a self-charged prototype photo-power pack for ensuring best performances under practical condition.

3.1. Characterization and optimization of SrF_2/PVDF NC film for LSESD

3.1.1. X-ray diffraction (XRD) analysis

The crystalline behaviour of the samples and the formation of SrF_2 NPs are investigated by X-ray diffraction technique as depicted in Fig. 2a. The formation of the nanosized SrF_2 NPs within the polymer matrix is confirmed by the peaks around 2θ = 26.7, 30.8, 44.2 and 52.4 corresponding to (111), (200), (220), (311) (JCPDS No. 06-0262) crystal planes in the XRD patterns of the NCs. Diffraction peaks at 2θ ~17.4° (100), 18.2° (020), 19.6°(021) and 26.3° ((201),(310)) are observed for pure PVDF which correspond to nonpolar α-crystallite.

The existence of prominent diffraction peak at 20.6° (020) in SrF_2/PVDF NC films confirms the nucleation of electroactive β-crystallites due to the catalytic effect of the SrF_2 NPs in PVDF matrix [27,28,31,32]. It is also noticeable that electroactive β polymorph nucleation in the SrF_2/PVDF NC films considerably increased with concentration of the SrF_2 NPs up to 16.4 vol %. The ratio of the intensity $I_{20.6}$ and $I_{18.2}$ (Fig. 2b) is calculated to measure the amount of *α and β* phase in the pure PVDF and SrF_2/PVDF NC films [33,34]. The maximum obtained value of this ratio is~ 9.01 for 16.4 vol % (PSR 0.15).

3.1.2. Fourier transform infrared spectroscopy

Fourier transform infrared (FTIR) spectra of pure PVDF and NPs

doped films are shown in Fig. 2c. From the spectrum of pure PVDF, the absorbance bands are observed at 489 cm^{-1} (CF_2 waging), 533 cm^{-1} (CF_2 bending), 615 and 764 cm^{-1} (CF_2 bending and skeletal bending), 795 and 975 cm^{-1} (CH_2 rocking) due to the α phase and a small absorbance band at 840 cm^{-1} (CH_2 rocking, CF_2 stretching and skeletal C–C stretching) which is for the β phase [26–28]. However, in the composite film, the α phase gradually diminishes and the electroactive β phase related characteristic absorbance bands became prominent at 475 cm^{-1} (CF_2 deformation), 510 cm^{-1} (CF_2 stretching), 600 cm^{-1} (CF_2 wag) and 840 cm^{-1} (CH_2 rocking, CF_2 stretching and skeletal C–C stretching) [35]. The intensity of the characteristic bands of β phase shows maximum at 16.4 vol % doping of SrF_2 NPs and then decreases for higher concentrations [36].

By using eqn (1), we have calculated the relative fraction of electroactive β phase content (F(β)) in the NPs doped PVDF films and the variation of F(β) (%) with dopant concentration has been illustrated (volume %) in the Fig. 2d [37,38]. The maximum F(β) value achieved is 80% for the 16.4 (volume %) doping concentration.

3.1.3. Thermal behaviours

The DSC thermographs of pure PVDF and SrF_2/PVDFNC samples are represented in Fig. 2e. Existence of a sharp melting peak at 163.1 °C for pure PVDF is due to the presence of α crystallite. The melting temperature has been shifted to higher temperature by ~ 3–4 °C for the NPs loaded PVDF films confirming the nucleation of β polymorphs [27,28,36]. This results are also well consistent with the data of FTIR and XRD. Further we have calculated the degree of crystallinity (X_c) of the films by evaluating the melting enthalpy (ΔH_m) of the samples from the DSC thermographs shown in Fig. 2f and g. Formation of electroactive β phase via strong electrostatic interaction between *in situ* synthesized SrF_2 NPs and the polymer chains enhance the degree of crystallinity and melting enthalpy with increase in concentration of the NPs and the highest X_c value ~66% is obtained for 16.4 vol % [39,40].

TGA thermographs of pure PVDF and SrF_2NPs modified PVDF thin films have been illustrated in Fig. 2h. A single mass loss has occurred at 430 °C for pure PVDF film. For the NPs doped PVDF films two stage mass losses are observed, one is between 229 °C to 349 °C and the second is around 448–460 °C [41]. The increment of the thermo-degradation temperature of about ~18–30 °C(second stage mass loss) shows a good thermal stability for the NCs.

3.1.4. Field emission scanning electron microscopy

Surface morphological and microstructural characterization of the unblended PVDF and *in situ* synthesized SrF_2 NPs incorporated PVDF films are studied in detail by the field emission scanning electron microscopy (FESEM) as shown in Fig. 3. The FESEM image of the pure PVDF thin film represents spherulites with diameter in the range~ 50–70 μm confirming the presence of the α polymorph in major amount. But for the NPs modified PVDF thin films, the presence of the comparatively smaller size spherulites (average diameter~ 10–15 μm) confirms the nucleation of the piezoelectric β polymorphs [42,43]. The formation of SrF_2 NPs (average diameter ~ 30–40 nm) in PVDF matrix are also confirmed by FESEM images. The NPs are grown in the PVDF matrix and uniformly distributed within the NC films upto 16.4 vol% (PSR0.15). Homogeneous growth and distribution of the SrF_2 NPs in the polymer matrix up to PSR0.15, leads to maximum electroactive β crystals due to optimum interfacial interaction between the NPs surfaces and the polymer chains. For higher loading concentration, agglomeration of NPs is observed within the polymer matrix thus reducing the interfacial interaction areas with the polymer chains.

3.1.5. Dielectric properties

The variation of the dielectric constant and tangent loss of samples as a function of SrF_2 NPs content at 20 Hz and 2 MHz are shown in Fig. 4a and b. The dielectric constant of the samples have been increased slowly upto PSR0.10 sample with increasing content of the NPs at 20 Hz and a sharp increment in dielectric value is observed at 16.4 vol% of SrF_2 NPs content indicating realization of percolation threshold value for the NC samples. For higher concentrations of the NPs the dielectric gradually decreases. However, the trend in dielectric pattern at 2 MHz is different (Fig. 4b) than at low frequency as dielectric properties at higher frequency is mainly dipolar. We have achieved a remarkable value of dielectric constant ~5.141 $\times 10^3$ for PSR0.15 at 20 Hz and 40 at 2 MHz for the same film which are 570 times and 10 times larger than that of the dielectric constant of the unblended PVDF film respectively. The tan δ values of the PSR thin films is increased almost linearly with the increasing SrF_2 content upto PSR0.15 and then decreases for both frequencies (Fig. 4a and b). This variation of the dielectric value may be explained by Maxwell–Wagner–Sillars (MWS) interfacial polarization [44–47]. Unification and localization of the charge carriers along with the mobilized ions increased at the interfaces of the NPs and PVDF matrix due to the inclusion of the conducting SrF_2NPs within the insulating plastic polymer which consequently lead to the giant enhancement of the dielectric value for the NC sample at a certain doping of the NPs i.e. percolation threshold value (16.4 vol %) [27,48]. The ac conductivity also increases with increasing SrF_2 NPs concentration in PVDF matrix up to 16.4 vol % and also with frequency (Fig. 4c).

Dependency of the dielectric constant, ac conductivity and tangent loss (tan δ) on the frequency of pure PVDF and NPs doped PVDF films are graphically illustrated in Fig. 4d–f. A decrease in the dielectric constant is observed for the SrF_2/PVDF NC samples with increasing frequency but the change in dielectric value with frequency for pure PVDF thin film is very low (Fig. 4d). This issue may be explained directly by the MWS principle [44,47]. The large dielectric constant value at lower frequency is mainly due to the existence of large interfacial polarization i.e., high surface accumulation of charges and the interaction between the short range dipoles at the conducting interfaces of the NCs under externally applied alternating electric field. When the frequency is increased, a restricted movement of the space charges and the low accretion of the charges with frequency within the samples result the failure of the MWS effect and reduction of dielectric value [44,48].

The dependence of the tangent loss (tan δ) with frequency is shown in Fig. 4e. A sharp increment in the tan δ value is seen up to a certain value and then the value sharply decreased with frequency i.e. the dielectric relaxation peaks are observed at different lower frequencies for the NPs modified PVDF thin films upto 16.4 vol % NPs concentration. This tan δ peaks or Debye-like relaxation process occurs in the samples due to large dielectric response at that frequency. The noticeable fact is that the tangent loss peaks are shifted towards higher frequency with increasing loading concentration of the NPs due to the strong dipolar relaxation associated with the SrF_2 NPs embedded in PVDF matrix [34,49]. The frequency dependency of ac conductivity of pure PVDF and SrF_2 NPs incorporated PVDF thin films are presented in Fig. 4f. The ac conductivity of the NPs loaded PVDF samples are almost invariant at low frequency region (20 Hz- 1 KHz) and then increased linearly at high frequency zone. The MWS effect and dipolar relaxation mode are the reason for the increment of the ac conductivity whereas the presence of frequency independent plateau is responsible for the constancy of conductivity i.e. dc conductivity at low frequency region. But, for pure PVDF the ac conductivity is increased with frequency throughout the frequency range suggesting purely ac plateau nature of the conductivity [27,34].

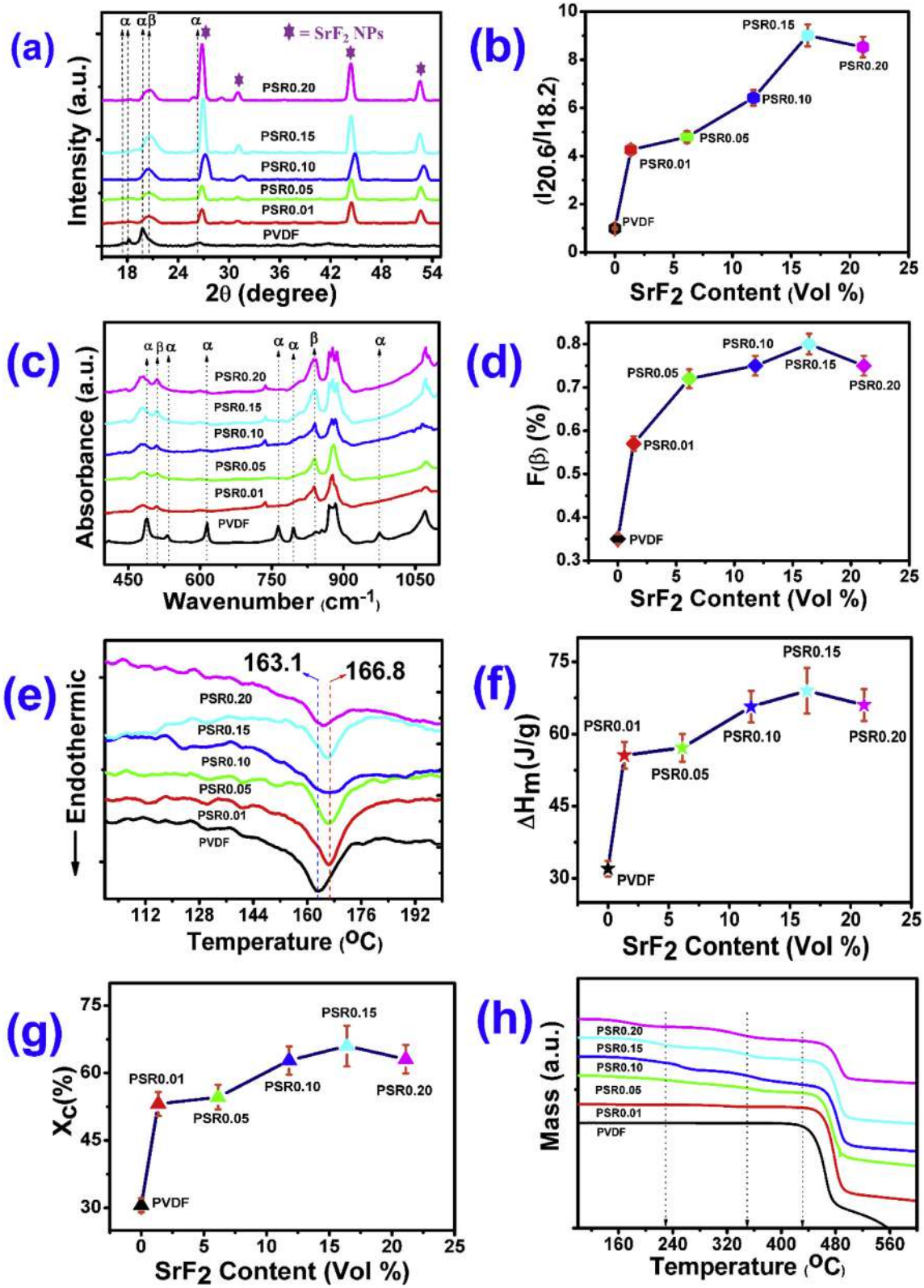

Fig. 2. (a) XRD patterns of pure PVDF and SrF_2 – PVDF NC thin films, (b) Ratio of $I_{20.5}$ and $I_{18.3}$ of the samples, (c) FTIR spectra of pure PVDF and PSR thin films, (d) β-phase content with increasing SrF_2 content form IR spectra, (e) DSC thermographs of pure PVDF and SrF_2 NPs incorporated PVDF thin films, the calculated (f) fusion enthalpy and (g) degree of crystallinity of the films from DSC thermographs and (h)TGA thermographs of pure PVDF and PSR samples for investing the thermal stability of the samples.

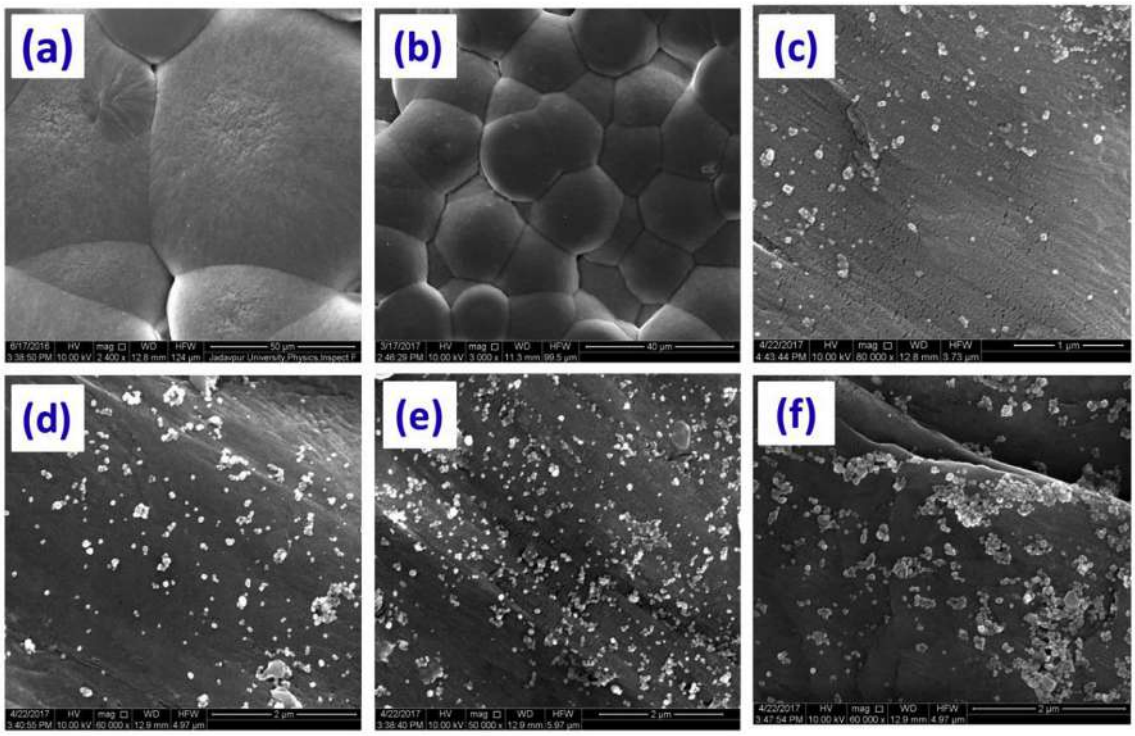

Fig. 3. FESEM images of (a) pure PVDF, (b) PSR0.01, (c) PSR0.05, (d) PSR0.10, (e) PSR0.15 and (f) PSR0.20 thin films.

3.2. Optical properties

Fig. 5a and b represent the UV–Vis and photoluminescence (PL) spectra of the samples respectively. A broad absorption peak centred at 215 nm (~5.76 eV) is observed for SrF_2NPs doped films with continuous increment of intensity with NP concentrations implying the uniform distribution and strong interaction between NPs and polymer matrix as shown in Fig. 5a. Whereas, no such characteristic peak was observed for the PVDF film in the UV–Vis spectrum. Fig. 5b, shows two strong peaks and a comparably slight small peak at 441 nm (blue), 536 nm (green) and 489 nm (blue) respectively at excitation wavelength $\lambda_{ex} = 202$ nm in the photoluminescence spectra of the NPs incorporated PVDF films. Due to the intimate and uniform conjugation of the SrF_2 NP within the polymer matrix, the intensity of the peaks gradually increased with the loading concentration of the NP. But for the same excitation wavelength, pure PVDF has no such characteristic peak. This UV absorption phenomenon of the composite films and corresponding blue and green emission (visible region) make this materials as a potential candidate for light emitting diode (LEDs), UV protector and sensor applications [50].

3.3. Mechanism and photovoltaic performances of the LSESD

Detailed characterization of the samples shows the PSR0.15 film as an appropriate candidate for device fabrication (Fig. 1) due to its superior dielectric value. The LSESD is fabricated by assembling a photoelectrode (FTO) involving phenosafranine-polyvinyl pyrrolidone with TiO_2 and ZnO NPs in the presence of ortho-phosphoric acid (H_3PO_4) as a photo-electrons generator, combined with the electroactive and high dielectric *in situ* synthesized SrF_2-PVDF NC thin film (PSR0.15) for photo-electron storage. Similarly, another device was also fabricated by replacing the PSR0.15 with pure PVDF film having same dimension. A 40 W tungsten bulb covered with ultra-violet and infrared light eliminator filters is used to charge the device with a power of 110 $mWcm^{-2}$.

Considering the working principle of dye-sensitized solar cell, the proposed mechanism of our device may be divided into two processes, generation of the photoelectrons and storage of the photo-generated charge carriers. The proposed working mechanism of our LSESD is schematically shown in Fig. 6a. A composite mixture of PSF-PVP-ZnO-TiO_2 dye solution in aqueous acidic medium (H_3PO_4) has been used as a solar part for photoelectron and hole generation by absorbing photons under light illumination. While the storage mechanism is mainly controlled by the electroactive and high dielectric PSR0.15 thin film of dimension 0.3 cm × 0.3 cm and thickness 15 μm. Here, FTO coated glass and aluminium acted as the working and counter electrode respectively. The HOMO/LUMO energy configuration of PSF, ZnO NPs, TiO_2NPs and UV–Vis absorption spectrum of the entire dye solution is shown in Fig. 6b and c respectively. Photoelectron generation activity by visible light (i.e. photons) determines the efficacy of the solar part i.e. the inorganic-organic dye composite film casted on the working electrode FTO. The combination of two NPs with PSF-PVP has been used as dye-sensitized solar part due to their excellent optoelectronic, photosensitivity and catalytic characteristics which are essential for improving the photons to electricity conversion efficiency of our prototype LSESD [51,52]. PVP and H_3PO_4 act as a solid polymer electrolyte and electron suppler within the dye film. [53].

When the device is introduced under visible light (~110 mW/cm^2), the PSF molecules are excited by absorbing photon ($h\nu$) and the electrons are jumped from HOMO state (~5.2 eV) to LUMO state of the PSF (~ -3.07eV). The excited photoelectrons are injected to the conduction band of TiO_2 (~ -4.21eV) NPs arising the oxidation of the dye molecule (PSF_{ox}).

$$PSF + h\nu \rightarrow PSF^* \rightarrow PSF_{ox} + e^-$$

Then, the injected photoelectrons in the conduction band of

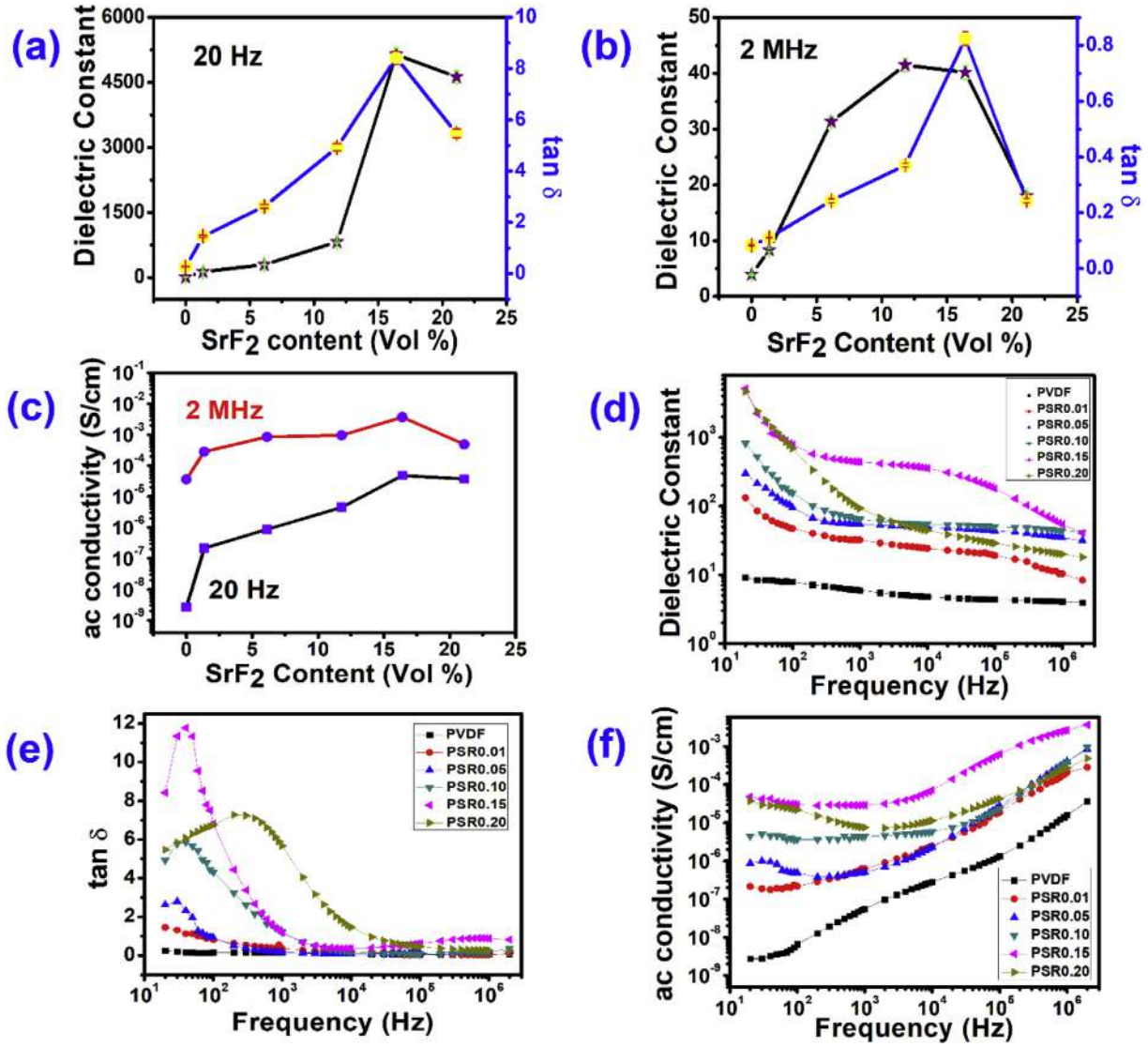

Fig. 4. Variation of dielectric properties of pure PVDF and SrF_2 NPs incorporated thin films with SrF_2 NPs content (a, b) dielectric constant and tangent loss and (c) ac conductivity. The frequency dependency of (d) dielectric constant, (e) tangent loss and (f) ac conductivity of the samples.

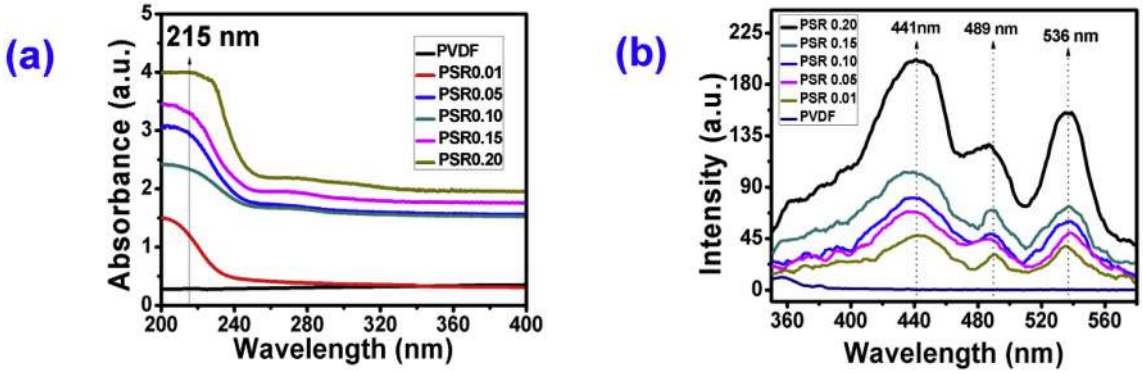

Fig. 5. (a) UV–Visible absorption spectra and (b) Photo luminescence spectra (λex = 202 nm) of pure PVDF and SrF_2 NPs doped PVDF thin films (PSR0.01, PSR0.05, PSR0.10, PSR0.15 and PSR0.20).

TiO_2 NPs defuse through the adjacent ZnO NPs (∼ − 4.3 eV) to FTO (∼ - 4.4eV). The main role of TiO_2 and ZnO NPs in solar unit are to tunnel the electrons through their conduction band to the FTO (Fig. 6b). Later, the electrons travel through the external circuit towards the counter electrode (Al) and accumulate at the junction between the Al and high dielectric PSR0.15 thin film as well as at

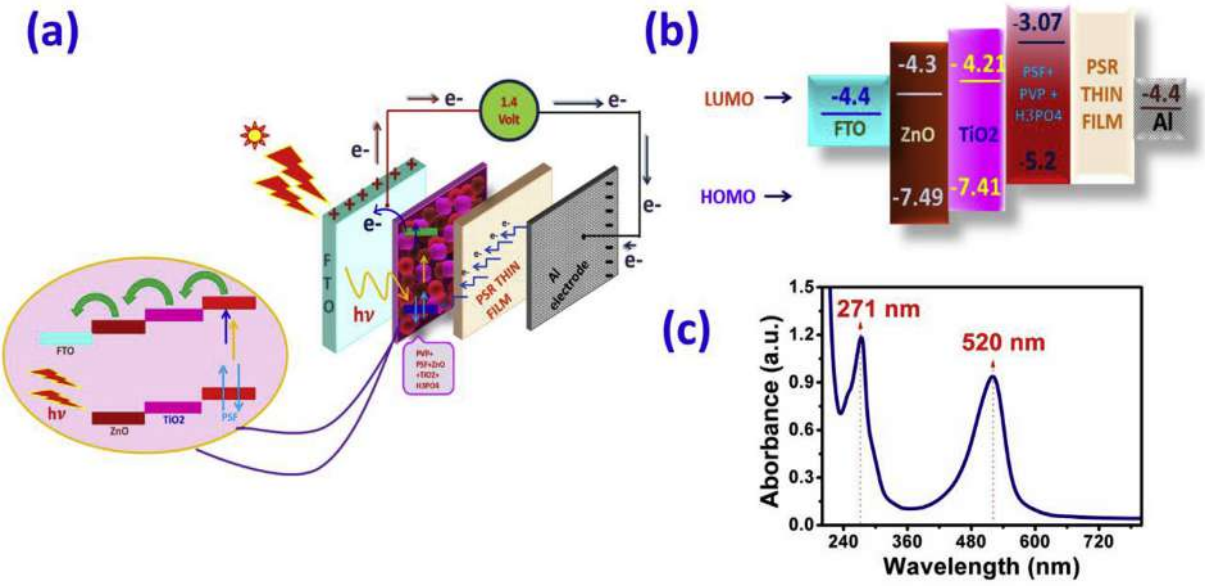

Fig. 6. (a) Schematic representation of the working mechanism of the LSESD. (b) HOMO and LUMO state of dye solution, (c) UV–Visible absorption spectrum of the dye-sensitized solar film or part.

the interfaces of the NPs and polymer matrix. Meanwhile, the photo-generated holes in PSF are replenished by the donating electrons from neighbouring solid polymer electrolyte film (PVP and H_3PO_4) which reduces the dye (PSF^+) to its ground state (PSF). In this process PVP and H_3PO_4 are oxidized.

$$PSF_{ox} + PVP \rightarrow PSF_{red} + PVP_{ox},$$
$$PSF_{ox} + H_3PO_4 \rightarrow PSF_{red} + [H_3PO_4]_{ox}$$

Continuous oxidation of PVP and H_3PO_4 drains the electrons resulting a net positive charge at the interfaces of the counter electrode and dielectric film (PSR0.15). And the counter electrode (Al) is negatively charged due to the large accumulation of the photo-electrons. Therefore, an effective potential difference is developed between the two electrodes which generates photo-voltage in photo-power cell [19,20,54–56]. When, the device is fully charged i.e. the open circuit voltage (V_{oc}) becomes ~ 1.48 V, the oxidized dye PSF^+ is ceased to be reduced back to its original state and the current flow in the device is dropped to zero. The current-voltage (J-V curves) and self-charging-discharging phenomena (V-t graph) of our LSESD are illustrated in Fig. 7a–d. A high short circuit current (I_{sc}) (~3.98 mA/cm^2) is measured during charging process for the LSESD containing PSR0.15 [57].

Whereas, I_{sc} is ~0.26 mA/cm^2 for pure PVDF based LSESD (Fig. 7a and b). Under light illumination, the open circuit voltage (V_{oc}) ~ 1.48 V is obtained within 1 min for the LSESD involving PSR0.15 as storage part which is 1.5 times larger than that of the pure PVDF based LSESD. Closer observation of the self-discharge curve (shown in Fig. 7c and d) signifies the superior storage stability of the PSR0.15 based photo-power cell than the pure PVDF based device as the V-t discharge characteristic is almost time independent for a long time. The discharge time i.e. internal electron recombination span is very low for the pure PVDF based device (Fig. 7d) due to the very small value of dielectric constant of the pure PVDF film. These lead to lower charge storage capacity and stability of that device for practical utilization. The internal discharging action of the photo-power cell is totally performed in a dark atmosphere.

In dark atmosphere, the photo-electrons generation process has been ceased as there is no photon to excite the PSF molecules. However, high dielectric PSR0.15 thin film behaves like an insulating medium and the lower conductivity nature of the PSR0.15 thin film allows very few electrons to pass through the insulating medium for recombination with holes. Thus a very small voltage drop and a small discharge current (~160 μA) is observed due to recombination of electrons and holes under this condition.

The performances of the two fabricated devices are investigated by discharging fully charged devices with a constant discharge current density ~1.64 mA/cm^2 for LSESD constructed using PSR0.15 and 1.07 mA/cm^2 formed using pure PVDF film under the dark ambient (Fig. 7e and f). The discharge time is found to be ~146 s and 12 s for the PSR0.15 and pure PVDF incorporated LSESD respectively. An estimated value of the stored charge density, specific areal capacitance, energy density and power density of our LSESD have been calculated from the discharge V-t graph (Fig. 7e and f)by using the following equations

$$Q = \int I_{dis} dt \tag{5}$$

$$C = Q/dV \tag{6}$$

$$E_{output} = \frac{1}{2} CV^2 \tag{7}$$

$$P = VI_{dis} \tag{8}$$

where, Q, C, E_{output}, P, I_{dis}, dt and dV are the charge density, specific areal capacitance, output energy density, power density, discharge current density, discharge time and voltage difference respectively. A highest charge storage capability of ~2400 C/m^2 has been achieved for our LSESD with PSR0.15 with superior energy and power density ~500 mW h/m^2 and~ 24.3 W/m^2 respectively (Fig. 8a). The storage ability i.e. specific areal capacitance(C) is found to be~ 1600 F/m^2 (Fig. 8a). These values are significantly high compared to previously reported photo-power units or photo-supercapacitors (See comparison in Table- S2 in supporting information). The output characteristics are also calculated for the device fabricated using pure PVDF film and shown in Fig. 8b.

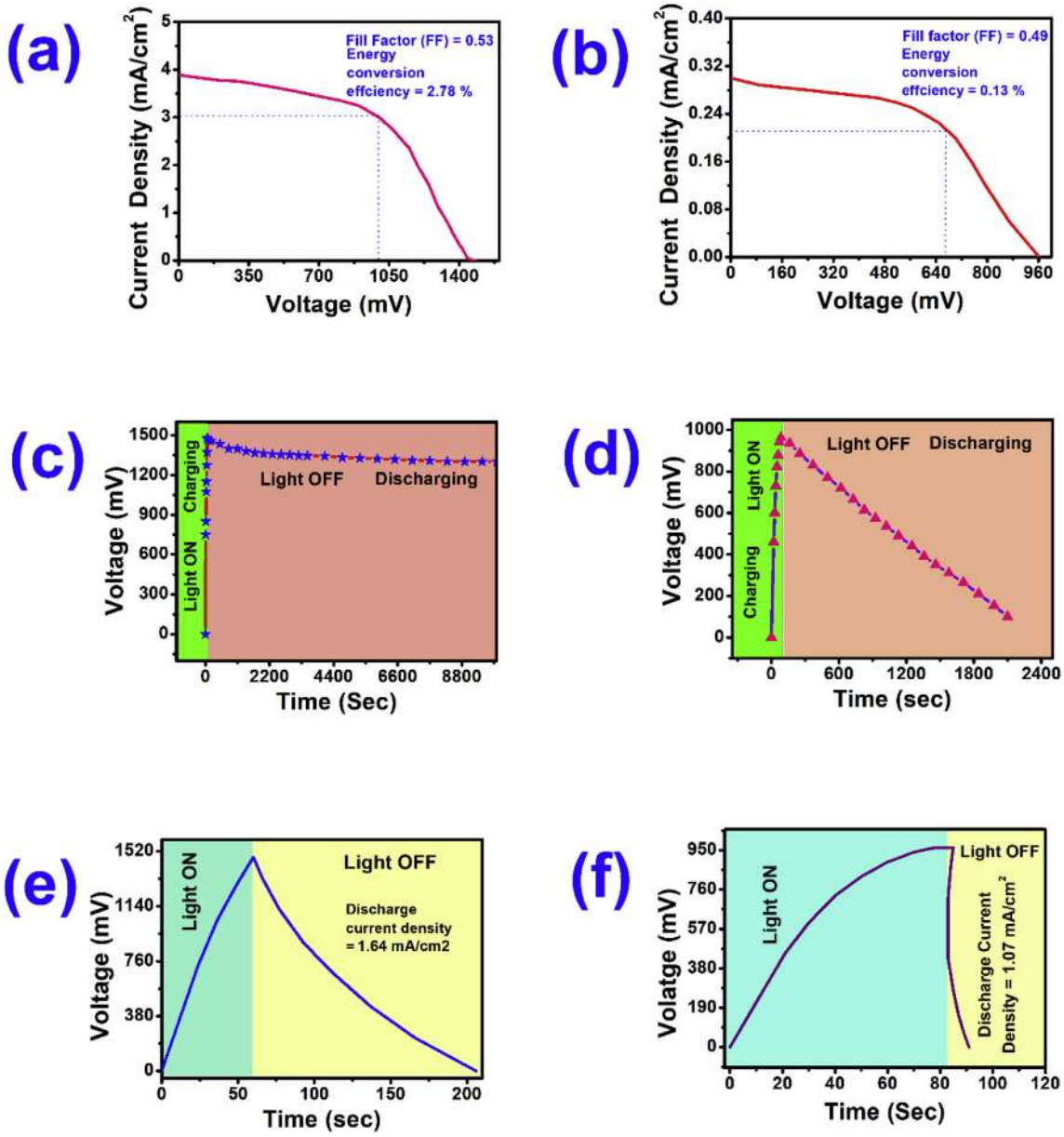

Fig. 7. (a, b)Current-Voltage (J-V) curves of PSR0.15 and pure PVDF based LSESDs, (c, d) Self-charging and spontaneous i.e. internal discharging behaviour (V-t curve) of PSR0.15 and pure PVDF based LSESDs as a function of time, and (e, f) Self-charging and discharging curve (V-t) in a constant current density of PSR0.15 and pure PVDF film based LSESDs as a function of time under light illumination and dark conditions.

To find out the energy conversion efficiency ($\eta_{conversion}$ %), we have used the following equation,

$$\eta_{conversion}\% = \frac{P_{out}}{P_{in}} \times 100 = \frac{V_{OC} \times I_{SC} \times FF}{P_{in}} \times 100 \quad (9)$$

V_{sc} = open circuit voltage, I_{SC} = short circuit current, FF = fill factor, P_{in} = the incident light power (110 mW/cm^2) [51].

$$\text{Where,} \quad FF = \frac{V_{pp} \times I_{pp}}{V_{OC} \times I_{SC}} \quad (10)$$

V_{pp} = voltage power point, I_{PP} = current power point, where I_{SC} and I_{PP} are in mA/cm^2, V_{OC} and $V_{pp}$are in V, P_{in} and P_{out} are in mW.

By using equations (7), (9), (11) and (12) the energy storage efficiency is evaluated as

$$\eta_{storage} = \frac{\eta_{overall}\%}{\eta_{conversion}\%} \quad (11)$$

$$\text{Overall efficiency,} \quad \eta_{overall}\% = \frac{E_{output}}{E_{input}} \times 100 \quad (12)$$

where the input energy density$E_{input} = P_{in} \times dt'$, dt' is the charging time [58].

The values of energy conversion, storage and overall efficiencies and the output characteristics (energy density, power density and storage ability) of the devices constructed with both PSR0.15 and pure PVDF thin films are graphically represented in Fig. 8c and d respectively.

We have achieved 92% energy storage efficiency associated with 2.78% energy conversion and 2.57% overall efficiency

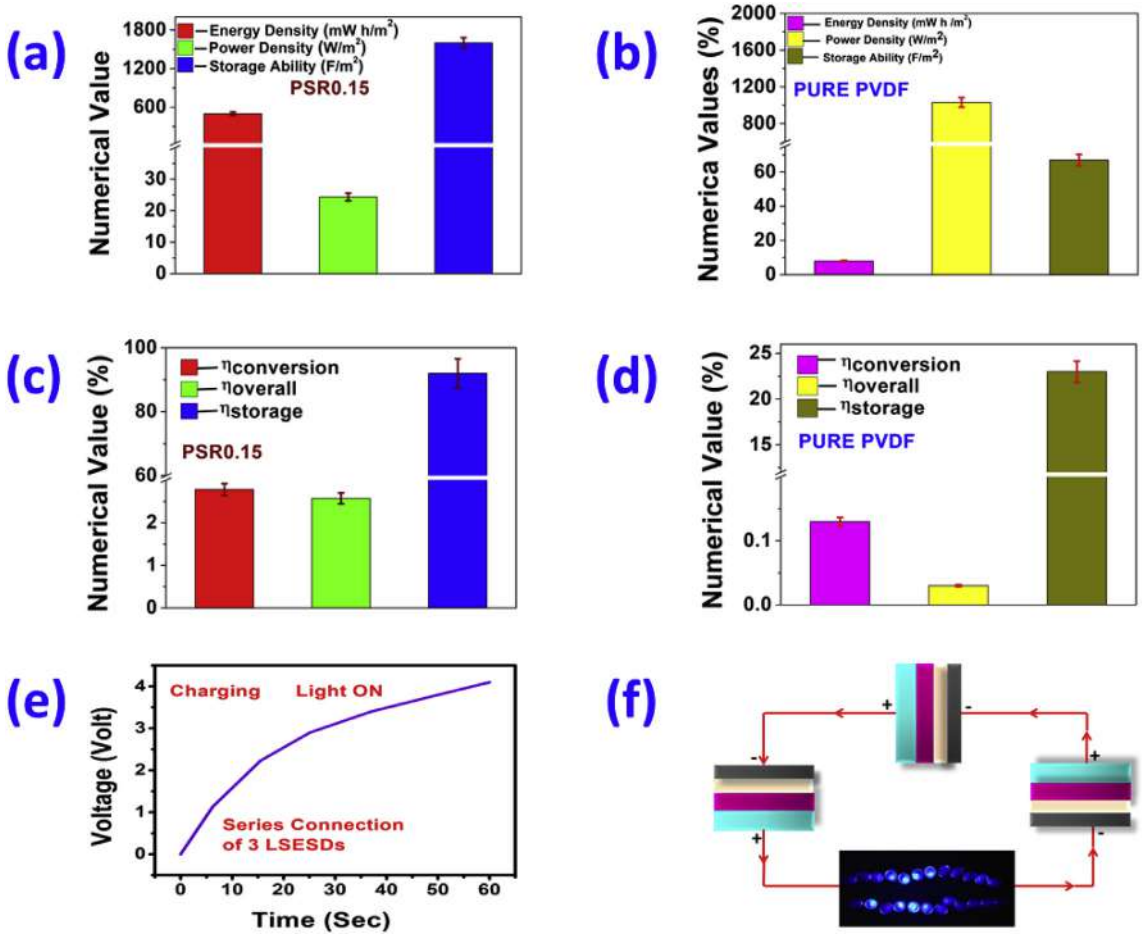

Fig. 8. (a,b) The energy density, power density and areal specific capacitances of the LSESD constructed using PSR0.15 and pure PVDF thin film respectively. (c, d) The conversion, overall and storage efficiencies of PSR0.15 and pure PVDF based LSESD respectively. (e) Self-charging (V-t) curve of three serially connected LSESDs with PSR0.15 thin film as storage part under light illumination and (e) Schematic diagram of the glowing of the blue LEDs by serially connected three PSESSs as a power bank.

(Illustrated in Fig. 8c) which are very promising and much better than the previously reported studies (Table S2). The efficiency values of PSR0.15 based LSESD are also many times larger than that of the efficiencies of the pure PVDF based LSESD (Fig. 8d). Our photo-power cell developed with PSR0.15 as storage part exhibits superior recyclability and storage stability for long times. We have investigated its performances for 12 weeks without any noticeable degradation in the output characteristics, storage ability and efficiencies. Finally to analyse the self-charging ability (V-t curve), storage stability and practical application as photo-power bank, we have connected three LSESD made of PSR0.15 serially. This serially connected combo pack have been charged upto ~4.1 V under light illumination within a short time span of 1 min (Fig. 8e). And the combo power bank is able to light up 24 serially connected blue LEDs continuously up to 10 days with same intensity demonstrated schematically in Fig. 8f and Video S1 (Supplied as supporting data). Here, we have used a fundamental and low cost technique to design a very simple and single hybrid self-charging energy storage device with very efficient energy creation and storage capability. This power pack has significant potential due to its superior performance and charge storing stability for acceptance in clean renewable energy developing areas for overcoming the daily energy demands.

Supplementary video related to this article can be found at https://doi.org/10.1016/j.electacta.2018.06.054.

4. Conclusions

In summary, we have grown SrF_2 NPs via *in situ* process within the PVDF matrix to develop a simple and cost-effective self-charged photo-power system efficient in energy harvesting and storage. *In situ* growth of SrF_2 NPs in PVDF matrix improves the electroactive β-phase formation (~80%) and the dielectric value of the PVDF from 9 to 5141. The maximum open circuit voltage ~1.48 V and short circuited current density (I_{sc}) ~ 3.9 mA/cm^2 are obtained from PSR0.15 based LSESD under the photo illumination with superior power density (~24.3 W/m^2) and storage capability (~1600 F/m^2). The maximum energy conversion, storage and overall efficiency of the self-charged LSESD are calculated to be ~2.78, 92 and 2.57% respectively. The storage potentiality of our LSESD is much higher than that of the earlier reported photo-induced power cells. We have also demonstrated the practical utilization of our photo-power unit lightening commercially available 24 blue LEDs with same intensity for 10 days by charging one time. Such high storage efficiency combined with stable reusable capacity of our self-charging photo-power cell has potential application possibilities in the field of portable and large scale energy demanding areas of our modern society.

Acknowledgement

We are thankful to Department of Higher Education, Science &

Technology and Biotechnology, Government of West Bengal, India and University Grants Commission (UGC) India for providing financial supports.

Appendix A. Supplementary data

Supplementary data related to this article can be found at https://doi.org/10.1016/j.electacta.2018.06.054.

References

[1] C. Shi, H. Dong, R. Zhu, H. LI, Y. Sun, D. Xu, Q. Zhao, D. Yu, Nano Energy 13 (2015) 670.
[2] M.C. Scharber, D. Mühlbacher, M. Koppe, P. Denk, C. Waldauf, A.J. Heeger, C.J. Brabec, Adv. Mater. 18 (2006) 789.
[3] C. Yuan, H.B. Wu, Y. Xie, X. W. (David). Lou, Angew. Chem. Int. Ed. 53 (2014) 1488.
[4] X. Huang, X. Zhang, H. Jiang, RSC Adv. 6 (2016) 96490.
[5] Y. Zi1, J. Wang1, S. Wang1, S. Li1, Z. Wen, H. Guo, Z.L. Wang, Nat. Commun. 7 (2016) 1.
[6] X. Fan, J. Chen, J. Yang, P. Bai, Z. Li, Z.L. Wang, Acsnano 9 (2015) 4236–4243.
[7] C. Wu, X. Wang, L. Lin, H. Guo, Z.L. Wang, ACS Nano 10 (2016) 4652–4659.
[8] J.P. Barton, D.G. Infield, IEEE Trans. Energy Convers. 19 (2004) 441.
[9] X.-L. Wu, L.-Y. Jiang, F.-F. Cao, Y.-G. Guo, L.-J. Wan, Adv. Mater. 21 (2009) 2710.
[10] C. Wu, X. Wang, L. Lin, H. Guo, Z.L. Wang, ACS Nano 10 (2016) 4652.
[11] V.L. Pushparaj, M.M. Shaijumon, A. Kumar, S. Murugesan, L. Ci, R. Vajtai, R.J. Linhard, O. Nalamasu, P.M. Ajayan, Proc. Natl. Acad. Sci. U. S. A. 104 (2007) 13574.
[12] T. Miyasaka, T.N. Murakami, Appl. Phys. Lett. 85 (2004) 3932.
[13] G. Wee, T. Salim, Y.M. Lam, S.G. Mhaisalkara, M. Srinivasan, Energy Environ. Sci. 4 (2011) 413.
[14] X. Zhang, X. Huang, C. Li, H. Jiang, Adv. Mater. 25 (2013) 4093.
[15] J. Xu, Y. Chen, L. Dai, Nat. Commun. 6 (2015) 8103.
[16] T.N. Murakami, N. Kawashima, T. Miyasaka, Chem. Commun. 26 (2005) 3346.
[17] F. Zhou, Z. Ren, Y. Zhao, X. Shen, A. Wang, Y.Y. Li, C. Surya, Y. Chai, ACS Nano 10 (2016) 5900.
[18] G. Wee, T. Salim, Y.M. Lam, S.G. Mhaisalkar, M. Srinivasan, Energy Environ. Sci. 4 (2011) 413.
[19] F. Khatun, N.A. Hoque, P. Thakur, N. Sepay, S. Roy, B. Bagchi, A. Kool, S. Das, Energy Technol. 5 (2017) 1.
[20] S. Roy, P. Thakur, N.A. Hoque, B. Bagchi, N. Sepay, F. Khatun, A. Kool, S. Das, Appl. Mater. Interfaces 9 (2017) 24198.
[21] X. Xue, P. Deng, S. Yuan, Y. Nie, B. He, L. Xing, Y. Zhang, Energy Environ. Sci. 6 (2013) 2615.
[22] Y.S. Kim, Y. Xie, X. Wen, S. Wang, S.J. Kim, H.K. Song, Z.L. Wang, Nano Energy 14 (2015) 77.
[23] J. Lee, J. Kim, J.Y. Kim, M.S. Hossain, S. Kim, J.H. Kim, J. Mater. Chem. A 4 (2016) 7983.
[24] L. Xing, Y. Nie, X. Xue, Y. Zhang, Nano Energy 10 (2014) 44.
[25] N.A. Hoque, P. Thakur, S. Roy, A. Kool, B. Bagchi, P. Biswas, M.M. Saikh, F. Khatun, S. Das, P.P. Ray, ACS Appl. Mater. Interfaces 9 (2017) 23048.
[26] Z.L. Wang, J. Song, Science 14 (2006) 242.
[27] P. Thakur, A. Kool, B. Bagchi, S. Das, P. Nandy, Phys. Chem. Chem. Phys. 17 (2015) 1368.
[28] P. Martins, A.C. Lopes, S. Lanceros-Mendez, Prog. Polym. Sci. 39 (2013) 683.
[29] A.V. Bune, V.M. Fridkin, S. Ducharme, L.M. Blinov, S.P. Palto, A.V. Sorokin, S.G. Yudin, A. Zlatkin, Nature 391 (1998) 874.
[30] Y. Yin, K. Feng, C. Liu, S. Fan, J. Phys. Chem. C 119 (2015) 8488.
[31] B. Adak, I. Chinyaac, S. Sen, RSC Adv. 6 (2016), 105137.
[32] S. Jiang, H. Wan, H. Liu, Y. Zeng, J. Liu, Y. Wu, G. Zhang, Appl. Phys. Lett. 109 (2016), 102904-1.
[33] B.P. Mandal, K. Vasundhara, E. Abdelhamid, G. Lawes, H.G. Salunke, A.K. Tyagi, J. Phys. Chem. C 118 (2014) 20819.
[34] P. Thakur, A. Kool, B. Bagchi, N.A. Hoque, S. Das, P. Nandy, Phys. Chem. Chem. Phys. 17 (2015) 13082.
[35] S. Lanceros-Méndez, J.F. Mano, A.M. Costa, V.H. Schmidt, J. Macromol. Sci.—-Phys. 40 (2001) 517.
[36] P. Costaa, J. Silvaa, b, V. Sencadasa, C.M. Costac, F.W.J. van Hattumb, J.G. Rochad, S. Lanceros-Mendeza, Carbon 47 (2009) 2590.
[37] P. Martins, C. Caparros, R. Goncalves, P.M. Martins, M. Benelmekki, G. Botelho, S. Lanceros-Mendez, J. Phys. Chem. C 116 (2012) 15790.
[38] S.P. Bao, G.D. Liang, S.C. Tjong, Carbon 49 (2011) 1758.
[39] P. Thakur, A. Kool, B. Bagchi, S. Das, P. Nandy, Appl. Clay Sci. 99 (2014) 149.
[40] P. Martins, C.M. Costa, J.C.C. Ferreira, S. Lanceros-Mendez, J. Phys. Chem. B 116 (2012) 794.
[41] D. Wu, L. Wu, G. Yu, B. Xu, M. Zhang, Polym. Eng. Sci. (2008) 1058.
[42] P. Thakur, A. Kool, B. Bagchi, N.A. Hoque, S. Das, P. Nandy, RSC Adv. 5 (2015) 28487.
[43] M. Wang, J.-H. Shi, K.P. Pramoda, S.H. Goh, Nanotechnology 18 (2007), 235701.
[44] Y. Li, X. Huang, Z. Hu, P. Jiang, S. Li, T. Tanaka, ACS Appl. Mater. Interfaces 3 (2011) 4396.
[45] Z.-M. Dang, L. Wang, H.-Y. Wang, C.-W. Nan, D. Xie, Y. Yin, S.C. Tjong, Appl. Phys. Lett. 86 (2005), 172905-1.
[46] F. Carpi, G. Gallone, F. Galantini, D.D. Rossi, Adv. Funct. Mater. 18 (2008) 235–241.
[47] A. Moliton, Applied Electromagnetism and Materials, Springer, New York, 2007 (chapter 3).
[48] R. Simoes, J. Silva, S. Lanceros-Mendez, R. Vaia, J. Mater. Sci. 45 (2010) 268.
[49] P. Lunkenheimer, V. Bobnar, A.V. Pronin, A.I. Ritus, A.A. Volkov, A. Loid, Phys. Rev. B 66 (2002), 052105.
[50] L. Luo, D. Bozyigit, V. Wood, M. Niederberger, Chem. Mater. 24 (2013) 4901.
[51] S.K. Mohapatra, N. Kondamudi, S. Banerjee, M. Misra, Langmuir 24 (2008) 11276.
[52] J.A. Anta, E. Guillen, R. Tena-Zaera, J. Phys. Chem. C 116 (2012) 11413.
[53] S. Hao, J. Wu, L. Fan, Y. Huang, J. Lin, Y. Wei, Sol. Energy 76 (2004) 745.
[54] A.P. Cohn, W.R. Erwin, K. Share, L. Oakes, A.S. Westover, Ra. E. Carter, R. Bardhan, C.L. Pint, Nano Lett. 15 (2015) 2727.
[55] P. Thakur, A. Kool, N.A. Hoque, B. Bagchi, F. Khatun, P. Biswas, D. Brahma, S. Roy, S. Banerjee, S. Das, Nano Energy 44 (2018) 456.
[56] M. Skunik-Nuckowska, K. Grzejszczyk, P.J. Kulesza, L. Yang, N. Vlachopoulos, L. Häggman, E. Johansson, A. Hagfeldt, J. Power Sources 234 (2013) 91.
[57] E. Kobayashi, Y. Watabe, R. Hao, T.S. Ravi, Appl. Phys. Lett. 106 (2015) 223504.
[58] Z. Liu, Y. Zhong, B. Sun, X. Liu, J. Han, T. Shi, Z. Tang, G. Liao, ACS Appl. Mater. Interfaces 9 (2017) 22361.